

# Deep unfolding architecture for MRI reconstruction enhanced by adaptive noise maps<sup>\*</sup>

Amir Aghabiglou<sup>1</sup>[0000-0001-6024-649X] and Ender M. Eksioglu<sup>2</sup>[0000-0002-7869-4159]

<sup>1</sup> Graduate School, Istanbul Technical University, Istanbul, Turkey  
aghabaiglou17@itu.edu.tr

<sup>2</sup> Electronics and Communication Engineering Department, Istanbul Technical University, Istanbul, Turkey  
eksioglu@itu.edu.tr

**Abstract.** Unfolding provides a potent method to improve deep network performance in image restoration problems. Recent results in the literature have demonstrated the improvement achieved by unfolding structures when compared to the non-unfolding singular use of a given network. Lately, unfolding models have been offered as promising solutions for the Magnetic Resonance Image (MRI) reconstruction problem. In this work we propose a novel deep unfolding structure for MR image reconstruction. We introduce an adaptive noise level parameter to the unfolding structure, inspired by the conventional iterative thresholding-based reconstruction models. The noise level parameter is calculated at each iteration using the error between the network output and the initial zero filling estimate. This new parameter is given as an additional input to the network, and it acts as an evolving regularizer for the image manipulation strength of the network over the unrolling iterations. The introduction of this adaptivity over iterations in the training step also improves the deep models' reconstructed image quality in the inference stage. Empirical results indicate that the recommended technique can converge to better reconstruction results when compared to state-of-the-art unfolding structures devoid of such an adaptive parameter. The introduction of the additional adaptive parameter results in an incremental increase in the parameter complexity, and the required reconstruction times also stand very similar. In this study, the statistical differences between developed techniques are investigated using the one-way ANOVA method. Additionally, a *t*-test is used to specify the major difference between the means of the two proposed structures. These results indicate that differences in the performance metrics results are statistically significant.

**Keywords:** Magnetic resonance imaging · MR Image Reconstruction · Deep learning · Unfolding deep networks.

---

<sup>\*</sup> This work was supported by TUBITAK (The Scientific and Technological Research Council of Turkey) under project no. 119E248.

## 1 Introduction

Magnetic Resonance Imaging (MRI) is an important modality in clinical imaging because of its non-invasive nature and capability of providing high-quality images, especially for soft tissues. However, it suffers from long data acquisition times [42]. To tackle this drawback, three major approaches for accelerating MR scans have been established. These mainstream approaches include faster imaging based on MRI physics, hardware modification by using multiple coils for parallel imaging, and signal processing techniques by reconstructing MR images from undersampled data acquisition. Much effort has been directed to speed up the scanning operation by utilizing undersampled k-space measurements [41, 17].

In last two decades, MRI reconstruction has extended from linear analytic reconstruction techniques like sensitivity encoding (SENSE) [29], GeneRalized Autocalibrating Partially Parallel Acquisitions (GRAPPA) [13] and Simultaneous Acquisition of Spatial Harmonics (SMASH) [37] to nonlinear iterative reconstructions methods including generalized series (GS) model [26], sparsity models [5], statistics distribution regularization [44], low-rank [14] and so on. Regularization based on sparsity or compressed sensing (CS) has been offered as a solution in image reconstruction with reduced measurements. CS-based on the sparsity prior has become a viable tactic for accelerating MRI in recent decades [27]. As another example in [39] patch-based transform learning was enhanced using extra global regularization terms. This particular technique incorporates both global regularization and patch-wise terms. The iterative optimization process used in CS-based reconstruction takes a long time to reach optimal results, and the regularization parameter selection is rather empirical. As a result, the computational complexity of these methods is quite high. Deep learning, on the other hand, is a subfield of machine learning that learns data patterns by employing multiple layers and can be used for both unsupervised and supervised training [20].

Deep learning lately has achieved tremendous breakthroughs, resulting in a lot of interest in different tasks. Image processing inverse problems like image segmentation [7, 46, 34] and image denoising [10, 18, 50] have greatly benefited from the deep learning tide. The popularity of deep learning methods is being elevated by advancements in computing capability and the development of novel network architectures. Some common deep learning arrangements can be named as convolutional neural network (CNN), U-Net [34], Multilayer perceptron (MLP) [40], residual network (ResNet), recurrent neural network (RNN) and generative adversarial network (GAN) [12].

Deep learning-based methods also find their way into the MR imaging field as a replacement for conventional model-based methods. With the groundbreaking progress in deep learning, the contribution of deep learning in MRI science appears to be continuously growing. Deep learning techniques have shown substantial gains in several aspects of MR imaging like MR image segmentation and reconstruction [23]. The advantage of residual connection has been introduced in a seminal study [22]. Subsequently, many studies [31, 32, 28, 11] were inspired by this successful application of the residual U-Net.

## 2 Related works

Recent deep models for MR image reconstruction have included unfolding-based techniques [36, 3, 24, 49, 43]. Unfolding strategies in deep learning usually begin with an assumed optimization problem the solution of which is a reconstructed image. Thereafter, they unfold the iterative optimization solution into a deep network. As an outcome, the steps arising from iterations are used to build the architecture of an unfolding-based model. CS reconstruction methodology is used in the majority of current unfolding-based deep-learning solutions. The deep-learning techniques based on unfolding provide an opportunity for a broader perception of the link between network architecture and efficiency [25]. The initial unrolling-based iterative network was offered by introducing the ADMM (Alternating Direction Method of Multipliers) network [4] in 2016.

Inspired by these successful applications, researchers introduced novel structures by unrolling networks like Iterative Shrinkage-Thresholding Algorithm (ISTA) under the title of ISTA-Net [48]. At almost the same time, similar structures including MoDL (Model-based reconstruction using Deep Learned prior) [2], cascade CNN [36], and variational network [15] have been introduced. Schlemper *et al.*'s cascade CNN network [36, 35] was one of these deep iterative structures that garnered prominence in tackling the inverse problem of MR image reconstruction. A Deep Cascade of Convolutional Neural Networks (DC-CNN) with data fidelity blocks is used in this proposed technique. The variational network [15] combined compressed sensing and deep learning methodologies to accelerate MR image reconstruction using an unrolled scheme. In [6], the author utilized a variational network for variable-density single-shot fast spin-echo MR imaging. Aggarwal *et al.* proposed MoDL [2] by including the DC layer inside a variational network to reconstruct MR images in an unrolled platform. In another study, PD-Net was offered by unfolding the primal-dual hybrid gradient (PDHG) pipeline [1] to solve inverse problems.

In [31] yet another unfolding structure is proposed for cardiac MR image reconstruction. Convolutional recurrent neural networks (CRNN) take advantage of spatial sequence dependencies as well as the iterative features of standard optimization techniques. The concatenation of U-Nets has been offered in [38] under the name of W-nets for MR image reconstruction. W-nets have been utilized in a dual-domain (image and k-space) approach. The author designed VS-Net (Variable splitting network) [9] by unfolding the obtained unrolling variable splitting optimization technique to implement a fast MR image reconstruction.

In another study, a self-attention deep network (SAT-Net) was suggested by utilizing a self-attention network and applying the data fidelity layer to the cartilage images [45]. Taking advantage of long-range dependencies, incorporating the DC layer and self-attention pathway into CNNs, effectually speeded up and improved their overall reconstruction result. Qiao *et al* [30] developed a compound unfolding architecture using the Approximate Message Passing (AMP) algorithm. Compared to other state-of-the-art MR image reconstruction techniques, they benefited from both model-based and data-based methodologies without using the weight-sharing policy in each CNN layer. FFDNet for the first

time is introduced by Kai Zhang *et al* [51] as a quick and flexible denoising CNN. The proposed denoiser, namely DRUNet, receives the noise level map as input and further incorporates residual blocks into the U-Net. Zhang *et al* [49] presented a Plug-and-Play Image Restoration (IR) model. Generally, plug-and-play IR entails two steps in an alternating iterative framework. The first step involves the solution of a data consistency sub-problem, and the second step ponders an image prior sub-problem. The Plug-and-play approach considers the use of standard denoisers to solve the image prior sub-problem. Hence, unlike conventional model-based techniques, plug-and-play IR can use advanced denoisers from the literature to implicitly specify the image prior.

In this work by getting inspiration from the recent unfolding structures, we tried to improve iterative unfolding network models’ performance by introducing a noise parameter  $\sigma_i$  adaptively calculated for each  $i^{\text{th}}$  iteration.  $\sigma_i$  is calculated using the dissimilarity between the reconstructed MR image at the  $i^{\text{th}}$  iteration and the original zero-filled (ZF). The addition of this parameter to the unfolding pipeline as an input feature map enhances the reconstruction performance considerably. This input acts as a regularizer for the network over the unfolding iterations. This additional feature map increases the overall complexity of the network only incrementally.

The rest of this article is organized as follows. In the first part of Section 3, the general framework of MR image reconstruction based on deep networks is discussed. The second part of section 3 introduces the contribution and innovation of this study in contrast to prior deep networks. The third part of section 3 delves into the specifics of the suggested innovative network architectures. Section 4 present the quantitative and qualitative results. Eventually, in the concluding part, the findings are summarized.

### 3 Proposed Approach

#### 3.1 General Framework

To accelerate MR image reconstruction, we need deep learning models to reconstruct images from undersampled datasets. Deep learning techniques learn from the difference between the reconstructed and gold-standard images to reconstruct MR images. As the initial procedure of the reconstruction process, we need to visualize the acquired data, namely undersampled k-space data using an inverse Fast Fourier Transform (IFFT):

$$y = \mathcal{F}_\Omega x_{\text{orig}} + n \tag{1}$$

$$x_{\text{zf}} = \mathcal{F}^{-1}y \tag{2}$$

Here,  $y$  can be defined as the undersampled data in the spatial domain.  $\mathcal{F}_\Omega$  is the encoding matrix or the subsampled Fourier transform function.  $n$  is disruption or noise created in the measurement process. The sequence of

selected points used in the MRI acquisition technique is described by  $\Omega$  and  $\Omega \in \{1, 2, 3, \dots, N\}^M$ . Here  $N \times M$  denotes the image total pixel size. The IFFT and real image is shown by  $\mathcal{F}^{-1}$  and  $x_{\text{orig}}$ , respectively.  $x_{\text{zf}}$  is the subsampled image. Before, feed forwarding the ZF image into the network we defined a zero-filled initial  $\sigma$  ( $\sigma_0$ ) and applied it as a second channel to the input. In fully sampled data,  $y$  fulfill the Nyquist sampling theorem and the MR image can be easily created using an inverse Fourier transform but in undersampled data, different techniques should be applied to address the non-determined properties resulting from undersampling. CS or deep learning methods can be one of these solutions.

$$\mathcal{F}_\Omega = U \mathcal{F} \quad (3a)$$

$$\mathcal{F}_\Omega = U \mathcal{F} S \quad (3b)$$

Here,  $U$  is the subsampling mask function.  $\mathcal{F}$  indicates the FFT and  $S$  denotes the sensitivity map for the multi-coil volumes. The MR image reconstruction template attempts to fill in missing points in the ZF image. In the training step, it seeks to learn by mitigating the difference between the output or reconstructed slice  $\tilde{x}$  and the target image. In this line, the target is to achieve the most cost-effective  $H$  function. As a result, the training step matches up with the following optimal solution:

$$\tilde{x} = H(x_{\text{zf}}) \quad (4)$$

$$\underset{\theta}{\operatorname{argmin}} \sum_{i=0}^{n_{\text{data}}} \|H_\theta(\tilde{x}^{(i)} - x^{(i)})\| \quad (5)$$

Here,  $H_\theta$  indicates the network quantified function, and  $\theta$  signifies the deep model's parameters.

The structural details of CNN and U-Net networks which have been utilized as baseline for all the developed frameworks are detailed in Table 1 and Fig. 1.

### 3.2 Proposed Structure

In this study, we introduce a new parameter  $\sigma$ . We calculate this parameter as follows:

$$\sigma_i = \frac{\|\tilde{x}_i - x_{\text{zf}}\|_F}{\sqrt{N \times M}} \quad (6)$$

In this regard, we calculated the  $\sigma$  within the Data consistency (DC) layer [8] and appended it to the DC layer output. The DC layer is implemented as follows:

$$x_{\text{out}} = \mathcal{F}^{-1}\{\overline{M} \circ (\mathcal{F}\tilde{x}) + y\} \quad (7)$$

**Table 1.** Structural details of baseline networks.

Network	Layer detail								
	# conv. layers	Initial layer detail			Middle layers detail		Reconstruction Layer detail		
CNN	5	Input Ch. size	1		Input Ch. size	64		Input Ch. size	64
		Output Ch. size	64		Output Ch. size	64		Output Ch. size	1
		Kernel size	3		Kernel size	3		Kernel size	3
		Stride	1		Stride	1		Stride	1
		Padding	1		Padding	1		Padding	1
		Bias	False		Bias	False		Bias	False
U-Net	5 downsampling block	Downsampling block				Upsampling block			
		1st conv. layer		2nd conv. layer		1st conv. layer		2nd conv. layer	
		Input Ch. size	n	Input Ch. size	n×2	Input Ch. size	n×2	Input Ch. size	n
		Output Ch. size	n×2	Output Ch. size	n×2	Output Ch. size	n	Output Ch. size	n
		Kernel size	3	Kernel size	3	Kernel size	3	Kernel size	3
	5 upsampling layers	Stride	1		Stride	1		Stride	1
		Padding	1		Padding	1		Padding	1
		Bias	False	Bias	False	Bias	False	Bias	False

Here,  $\overline{M}$  is the inverse of the subsampling function that was used to undersample the raw data.  $\circ$  is used for performing the point-wise product, and  $y$  is addressed in (1).

In a nutshell, the proposed adaptive noise level parameter, in addition to all other parameters, travels through and gets updated in each iteration of the unfolding structure. Thereafter, the optimizer function minimizes the error between the last network output and input dirty image based on these updated parameters.

### 3.3 Architecture

In this study, we have taken advantage of two state-of-the-art variants of U-Net and CNN for MRI reconstruction. The conventional unfolding structure and the proposed unfolding structure are represented in Fig. 2. As shown in Fig. 2, initially ZF image is created by applying IFFT to the undersampled k-space data. After calculating the absolute value of input tensors, ZF images are normalized. All images are then center-cropped to  $320 \times 320$  pixels to ensure that all slices from the dataset are the same size. Same as Fig. 2, these two models were unfolded by performing five iterations over each network and implementing the DC layer to each network output.

**CNN based networks** Regarding CNN implementations, a CNN architecture similar to the one used in [36, 3] is chosen. The model includes five convolutional layers. ReLU activation function was applied inside these layers. In this layout, the channel sizes in the initial and reconstruction layers are both set to two. In all convolutional layers, the feature map sizes are arranged as 64. In all layers, the kernel size, stride, and padding size are set to be three, one and one, respectively. This model was converted to a residual model in order to get a better reconstruction result. The Adam optimizer is chosen with a learning rate of  $10^{-4}$  and a weight decay of  $10^{-7}$ .

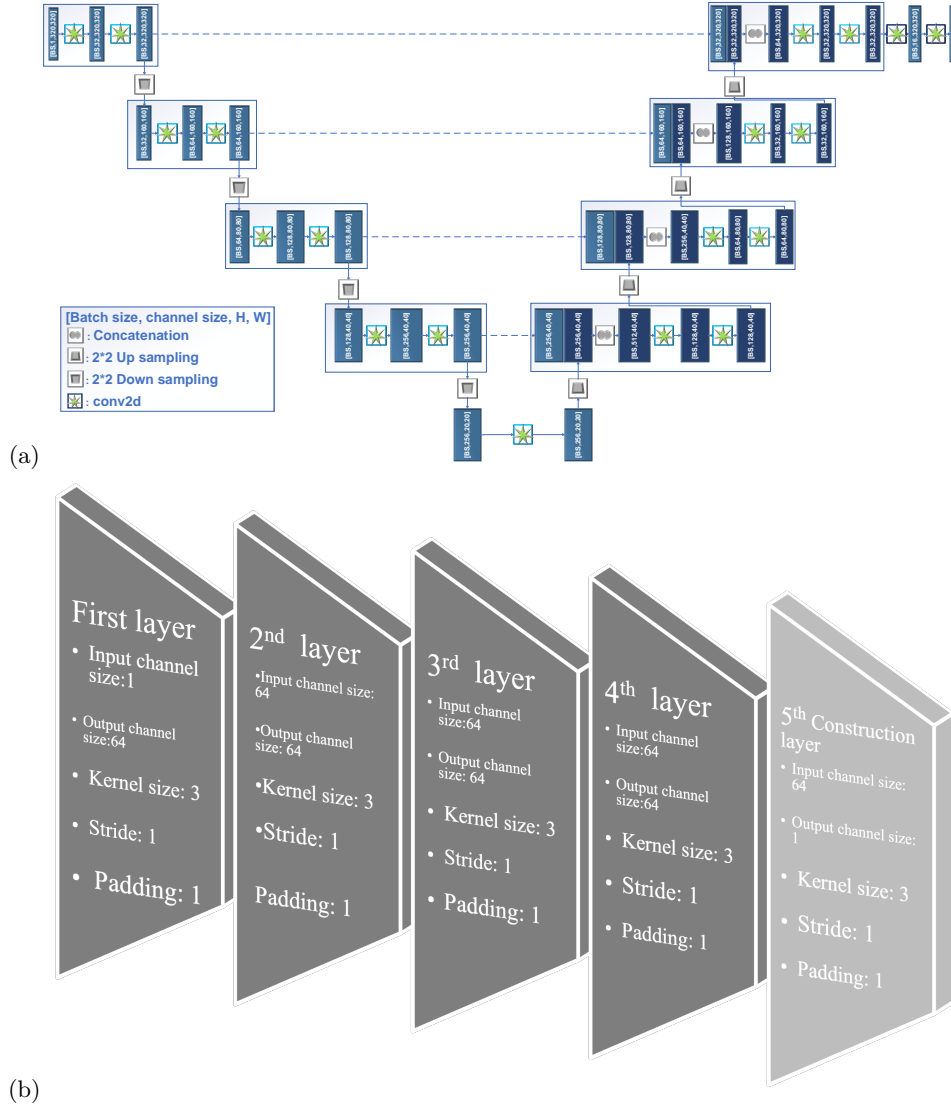
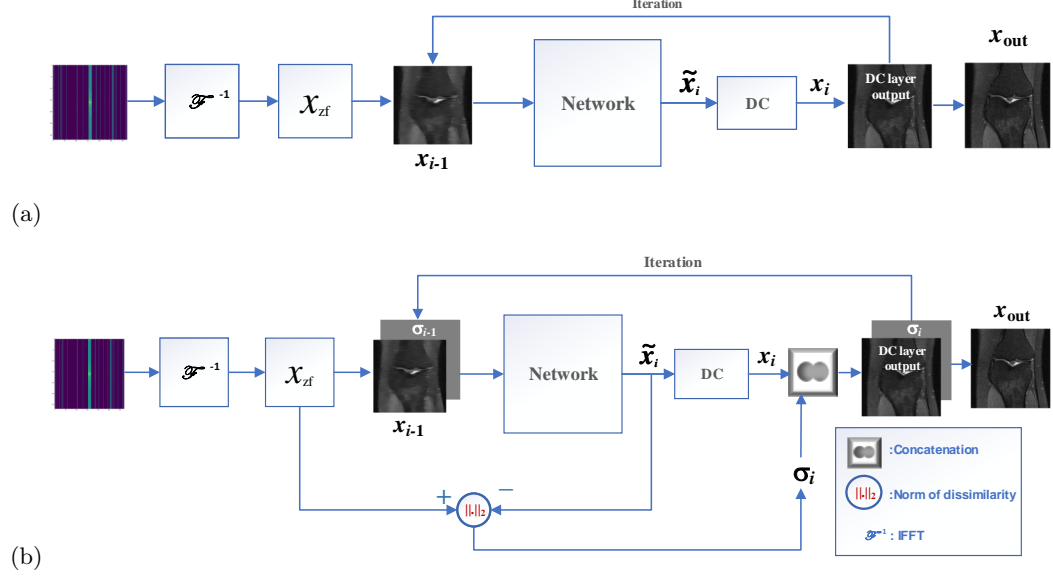


Fig. 1. Detailed outlines of the baseline networks. (a) U-Net. (b) CNN.

**U-Net based networks** For U-Net based frameworks simulations, we used the arrangement released by the Facebook AI Research (FAIR) team [47]. This architecture includes downsampling and upsampling steps. Each of these steps consists of two  $3 \times 3$  convolutional layers which are activated by ReLU. The contraction layer applies average pooling for halving the feature map's size. The expanding layer doubles the size of feature maps using the 2D transposed convolutional layer. The reconstruction layer includes a  $1 \times 1$  convolutional layer for



**Fig. 2.** Unfolding networks for MRI reconstruction. (a) Conventional unfolding structure. (b) Proposed unfolding structure.

generating an image with two channels. The U-Net model reconstruction loss is quantified using the mean absolute error (L1 loss) and it is optimized using the Root Mean Squared Propagation (RMSprop). The dropout probability is considered to be zero. The number of pooling layers is configured to four.

In Algorithm 1, we provide an algorithmic description for the proposed unfolding structure described in this article. Here,  $\mathcal{N}$  is the network that has an additional input in the form of the noise level parameter  $\sigma$ .  $x_i$  on the other hand, indicates the data consistency layer output.  $\|\cdot\|_F$  is the matrix Frobenius norm.  $N$  and  $M$  denote the dimensions of the target image.

```

Initialization:  $\sigma_0, x_0 = x_{zf}$ 
for  $i = 1 : n - 1$  do
   $\tilde{x}_i = \mathcal{N}_{\sigma_{i-1}}(x_{i-1})$ 
   $\sigma_i = \frac{\|\tilde{x}_i - x_{zf}\|_F}{\sqrt{N \times M}}$ 
   $x_i = \text{DC}(\tilde{x}_i, y)$ 
end for
 $x_{out} = x_n$ 

```

**Algorithm 1:** The steps for proposed unfolding structure.

### 3.4 Simulation Setting

**Experimental setup** Python 3.6 was used in conjunction with Pytorch 1.4.0. The training was implemented by using two GeForce RTX 2080Ti GPUs, each with 11GB of RAM. All models in this study, including suggested and state-of-the-art networks, were trained for 20 epochs, which was found to be sufficient for all model simulations.

**Evaluation Methodology** In this study, we evaluated developed models' performance using three metrics of performance, namely Peak Signal to Noise Ratio (PSNR), Normalized Mean Squared Error (NMSE), and Structural Similarity Index Measure (SSIM). PSNR is the ratio of the signal's highest achievable power to the power of the distorting noise that influences the quality of its depiction. Therefore, PSNR between the real image  $G_t$  and network output image  $R_i$  can be given as follow.

$$\text{PSNR}(R_i, G_t) = 10 \log_{10} \frac{\max(G_t)^2}{\text{MSE}(R_i, G_t)} \quad (8)$$

The MSE indicates the mean square error. On the other hand, the NMSE index is computed by calculating the pixel-by-pixel difference between the real and reconstructed images.

$$\text{NMSE}(R_i, G_t) = \frac{\|R_i - G_t\|_2^2}{\|G_t\|_2^2} \quad (9)$$

$\|\cdot\|_2^2$  is the squared Euclidean norm. Additionally, SSIM generally is addressed between two patches of an image.

$$\text{SSIM}(P_1, P_2) = \frac{(2\mu_{P_1}\mu_{P_2} + C_1)(2\sigma_{P_1 P_2} + C_2)}{(\mu_{P_1}^2 + \mu_{P_2}^2 + C_1)(\sigma_{P_1}^2 + \sigma_{P_2}^2 + C_2)} \quad (10)$$

Here,  $\sigma_{P_1}^2$  and  $\sigma_{P_2}^2$  are pixel variances related to  $P_1$  and  $P_2$ , respectively. The average values for  $P_1$  and  $P_2$  are denoted as  $\mu_{P_1}$  and  $\mu_{P_2}$ , respectively. The covariance value is indicated as  $\sigma_{P_1 P_2}$ .  $C_1$  and  $C_2$  are stabilizer of the division and can be calculated as follow.

$$C_1 = (0.01L)^2 \quad (11a)$$

$$C_2 = (0.03L)^2 \quad (11b)$$

Here,  $L$  is equal to the maximum pixel value of the ground truth image. The superior performance of models is expressed by higher PSNR and SSIM and lower NMSE magnitudes.

**Dataset** In a variety of applications, deep convolutional networks have outperformed state-of-the-art approaches. As a consequence, deep learning-based approaches have become increasingly popular; but the availability of training datasets limits their improvements [19, 34, 21]. Until now, different methods and training datasets were provided in the literature to tackle this limitation. Among these novelties, the fastMRI dataset is a fresh and rather a comprehensive form of an MR image dataset designed towards MR image reconstruction [47]. This collection contains data for numerous types of MR images in a number of forms. Images of single and multiple coils are included inside this dataset. The data includes the fully sampled k-domain slices, image domain, and DICOM format images. The single-coil image type of this dataset is used in this study. Table 2 summarize data distribution in this collection. The fastMRI dataset contains 1372 volumes and 49085 slices of single-coil MRI. These volumes are separated into subsets of training, validation, test, and challenge. Each volume provides fully sampled slices both in image and k-domain. In this study, the simulation started by undersampling the k-domain slices with a random Cartesian subsampling function with 4-fold and 8-fold acceleration factors. Subsequently, subsampled data were transferred into the image domain by applying IFFT.

**Table 2.** Volume and slice distribution in the fastMRI single-coil dataset [47].

Subset name	Volumes	Slices
Training	973	34742
Validation	199	7135
Test	108	3903
Challenge	92	3305

## 4 Experimental Results

### 4.1 Quantitative Results

In this paper, we have proposed a novel trainable parameter. We enforced this parameter into the unfolding structure of state-of-the-art pipelines. Random Cartesian subsampling functions with 4-fold and 8-fold acceleration factors were used to undersample the fully-sampled slices in the k-domain. The results of developed simulations and their standard deviations are reported in Tables 3 and 4 for two undersampling acceleration factors. The proposed novelty improved reconstruction results based on PSNR, NMSE, and SSIM indices. The time for reconstruction of 32 slices using developed models is provided. These reconstruction times are appropriate for real-time clinical applications.

In this work, we used statistical evaluation tools to assess the acquired quantitative results. To do so, one-way analysis of variance tryouts and paired *t*-tests were used to confirm the statistical significance of the simulated models in terms

**Table 3.** Simulation results for fastMRI dataset undersampled with 4-fold random Cartesian mask.

Acceleration Network	4-fold				#Parameter	Time (s)
	Loss	NMSE ( $\times 10^{-3}$ )	SSIM( $\times 10^{-3}$ )	PSNR		
ZF	-	41.679	711.59	29.876	-	-
CNN [36]	0.308	34.259 $\pm$ 17.43	755.65 $\pm$ 78.76	30.880 $\pm$ 2.49	111,744	0.095
k-space DL [16]	0.257	32.060 $\pm$ 18.92	763.45 $\pm$ 79.35	31.273 $\pm$ 2.66	7,756,418	0.173
KIKI-net [11, 33]	0.291	31.297 $\pm$ 17.33	766.52 $\pm$ 81.23	31.419 $\pm$ 2.78	1,168,128	0.78
Deep Cascade CNN [36]	0.280	26.520 $\pm$ 18.61	790.00 $\pm$ 85.15	32.412 $\pm$ 3.14	111,744	0.417
<b>Unfolding CNN with <math>\sigma</math></b>	0.274	<b>25.225<math>\pm</math>17.38</b>	<b>797.65<math>\pm</math>82.30</b>	<b>32.762<math>\pm</math>3.29</b>	112,896	0.487
U-Net [47, 3]	0.281	26.821 $\pm$ 18.18	785.93 $\pm$ 86.16	32.419 $\pm$ 3.17	7,756,097	0.15
Unfolding U-Net [3]	0.261	22.489 $\pm$ 17.29	813.83 $\pm$ 83.73	33.585 $\pm$ 3.72	7,756,097	0.913
<b>Unfolding U-Net with <math>\sigma</math></b>	0.260	<b>22.360<math>\pm</math>17.28</b>	<b>815.62<math>\pm</math>83.71</b>	<b>33.631<math>\pm</math>3.74</b>	7,756,418	1.032

**Table 4.** Simulation results for fastMRI dataset undersampled with 8-fold random Cartesian mask.

Acceleration Network	8-fold				#Parameter	Time (s)
	Loss	NMSE ( $\times 10^{-3}$ )	SSIM ( $\times 10^{-3}$ )	PSNR		
ZF	-	77.751	603.37	26.921	-	-
CNN [36]	0.451	69.277 $\pm$ 19.88	637.76 $\pm$ 100.66	27.462 $\pm$ 2.01	111,744	0.095
KIKI-net [11, 33]	0.431	62.103 $\pm$ 19.41	644.20 $\pm$ 103.54	28.020 $\pm$ 2.11	1,168,128	0.78
k-space DL [16]	0.437	58.376 $\pm$ 21.89	651.80 $\pm$ 103.98	28.292 $\pm$ 2.07	7,756,418	0.174
Deep Cascade CNN [36]	0.417	54.785 $\pm$ 22.32	655.84 $\pm$ 112.67	28.639 $\pm$ 2.20	111,744	0.417
<b>Unfolding CNN with <math>\sigma</math></b>	0.405	<b>50.772<math>\pm</math>22.59</b>	<b>670.04<math>\pm</math>113.30</b>	<b>29.037<math>\pm</math>2.30</b>	112,896	0.487
U-Net [47, 3]	0.380	43.275 $\pm$ 23.47	692.96 $\pm$ 118.22	29.952 $\pm$ 2.55	7,756,097	0.15
Unfolding U-Net [3]	0.356	35.791 $\pm$ 24.64	715.45 $\pm$ 125.47	31.185 $\pm$ 3.19	7,756,097	0.913
<b>Unfolding U-Net with <math>\sigma</math></b>	0.355	<b>35.589<math>\pm</math>24.43</b>	<b>717.78<math>\pm</math>124.31</b>	<b>31.267<math>\pm</math>3.12</b>	7,756,418	1.032

of all evaluation indices and configurations. In this setup, the threshold  $p$ -value is set as  $\alpha = 0.05$ . In Table 5, the ANOVA test findings reveal more than 99% reliability for both of acceleration factors and all evaluation metrics. As indicated in result section of Table 5, the null hypothesis, which states that the population means of the different networks are identical, is rejected. In addition, the effectiveness of the proposed models was assessed pair-wised in comparison to that of state-of-the-art structures by  $t$ -test. The paired  $t$ -tests yielded  $p$ -values less than the threshold value of 0.05, indicating more than 95% reliability in our suggested structures.

**Table 5.** ANOVA (one-way analysis of variance).

Acceleration factor	$p$ -value			Result
	NMSE	SSIM	PSNR	
4x	3.01E-10	2.71E-14	1.34E-20	$H_0$ rejected
8x	2.43E-45	1.06E-12	2.33E-48	$H_0$ rejected

Additional MRI reconstruction experiments have been also performed using a non-Cartesian down-sampling mask. We have retrained the deep learning methodologies for the case of a 4-fold acceleration factor when using a non-Cartesian, namely radial sampling mask. The results of the different methods for the radial mask sampling case are given in Table 6. The results in Table 6 show that the methods proposed in this study can maintain their superior reconstruction performance in the case of a non-Cartesian sampling mask. The performance robustness of the proposed model is approved by the application of a different type of undersampling mask function. As we expected from the result table related to the random Cartesian mask function, the concatenation of the adaptive noise level map again improved the result of cutting-edge unfolding structures.

**Table 6.** Simulation results for fastMRI dataset undersampled with 4-fold radial mask.

Acceleration factor		4-fold			#Parameter	Time (s)
Network	Loss	NMSE( $\times 10^{-3}$ )	SSIM( $\times 10^{-3}$ )	PSNR		
ZF	-	37.483	731.15	30.344	-	-
CNN [36]	0.317	32.491 $\pm$ 15.90	765.49 $\pm$ 75.55	31.052 $\pm$ 2.35	111,744	0.102
U-Net [47, 3]	0.276	24.041 $\pm$ 17.81	793.97 $\pm$ 89.45	33.121 $\pm$ 3.43	7,756,097	0.156
k-space DL [16]	0.270	23.218 $\pm$ 17.07	803.26 $\pm$ 82.52	33.235 $\pm$ 3.36	7,756,418	0.170
Deep Cascade CNN [36]	0.259	20.976 $\pm$ 16.90	820.10 $\pm$ 85.79	34.017 $\pm$ 3.87	111,744	0.421
<b>Unfolding CNN with <math>\sigma</math></b>	0.257	<b>20.565<math>\pm</math>16.76</b>	<b>824.16<math>\pm</math>84.66</b>	<b>34.184<math>\pm</math>3.96</b>	112,320	0.539
Unfolding U-Net [3]	0.254	20.128 $\pm$ 16.70	828.96 $\pm$ 84.47	34.361 $\pm$ 4.08	7,756,097	0.945
<b>Unfolding U-Net with <math>\sigma</math></b>	0.253	<b>20.121<math>\pm</math>16.71</b>	<b>830.80<math>\pm</math>84.66</b>	<b>34.458<math>\pm</math>4.07</b>	7,756,418	0.987

In Fig. 3, the  $\sigma$  evolutions are given for each iteration of the novel unfolding structure in the case of random Cartesian sampling. In this figure, each point indicates the average  $\sigma$  value for all slices of the full dataset in a specified epoch of training. It can be inferred that the  $\sigma$  value evolves through each iteration and training epoch in a regular fashion. Moreover, the  $\sigma$  value also evolves in the test phase. The evolution of  $\sigma$  over the test iterations significantly overlaps with the final  $\sigma$  values obtained in the training phase.

The PSNR and SSIM evolution also are given in Figs. 4 and 5 over each iteration of the unrolling paradigm with  $\sigma$ . Fig. 6 depicts the improvement detail in each iteration. It can be inferred from Figs. 4, 5 and 6 that the image quality increases over the unfolding iterations. Around epochs 15 to 20 the network seems to converge to the best solution.

Additionally, cross-validation has also been applied on the fastMRI dataset to verify the performance consistency of the proposed technique. In this regard, 12-fold cross-validation has been applied to all of the proposed and compared networks when using the fastMRI dataset. It has been observed that the proposed novel structure maintained its performance improvement in comparison to the competing pipelines in this cross-validation setting also.

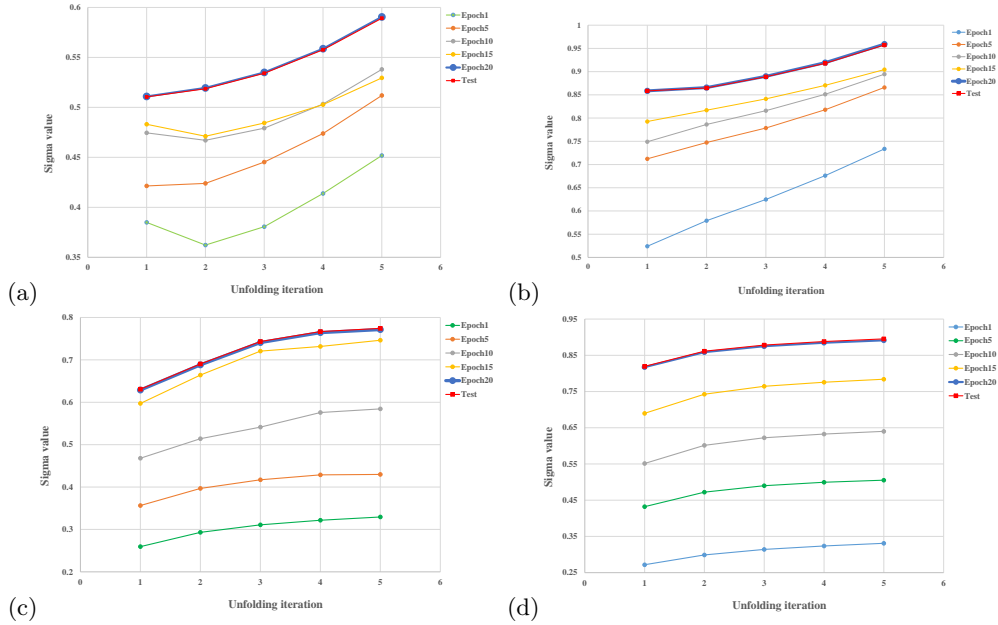


**Fig. 3.** Sigma evolution during the iteration. (a) Unfolding CNN for 4-fold acceleration factor. (b) Unfolding CNN for 8-fold acceleration factor (c) Unfolding U-Net for 4-fold acceleration factor. (d) Unfolding U-Net for 8-fold acceleration factor.

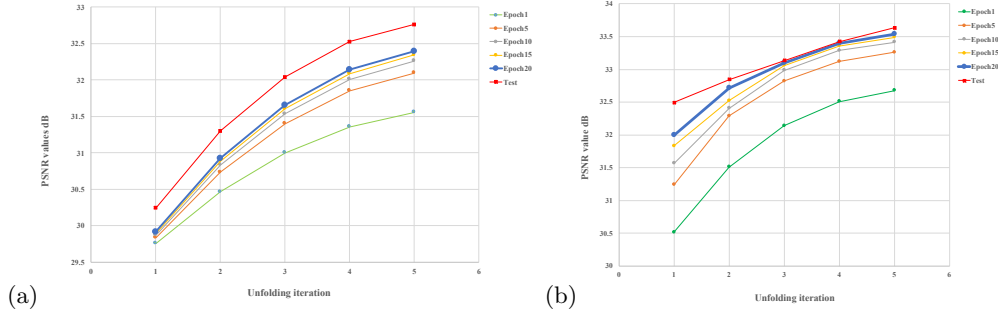


**Fig. 4.** PSNR evolution during iterations. (a) Unfolding CNN with  $\sigma$  for 4-fold acceleration factor. (b) Unfolding U-Net with  $\sigma$  for 4-fold acceleration factor.

## 4.2 Qualitative Results

This section provides a visualized analogy between the proposed novel structures and state-of-the-art networks. Fig. 7 depicts a specific slice in the k-domain and subsampled representations of the same slice with 4-fold and 8-fold acceleration factors with random Cartesian mask function. One particular reconstructed image from the test sample is displayed in this section. The suggested models' performance was assessed by making a comparison of their generated images.

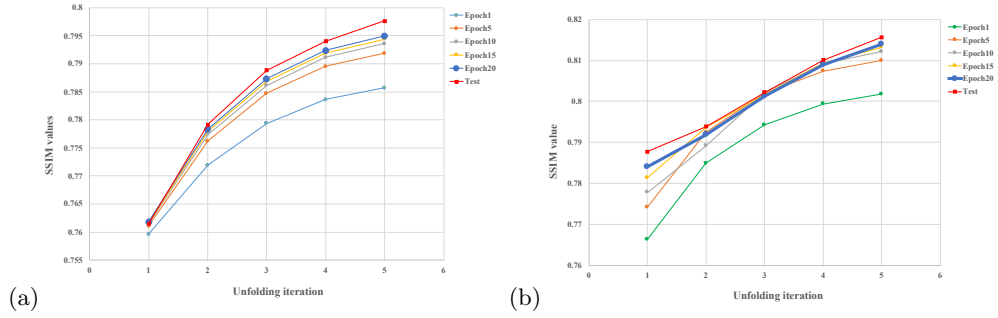


**Fig. 5.** SSIM evolution during iteration. (a) Unfolding CNN with  $\sigma$  for 4-fold acceleration factor. (b) Unfolding U-Net with  $\sigma$  for 4-fold acceleration factor.

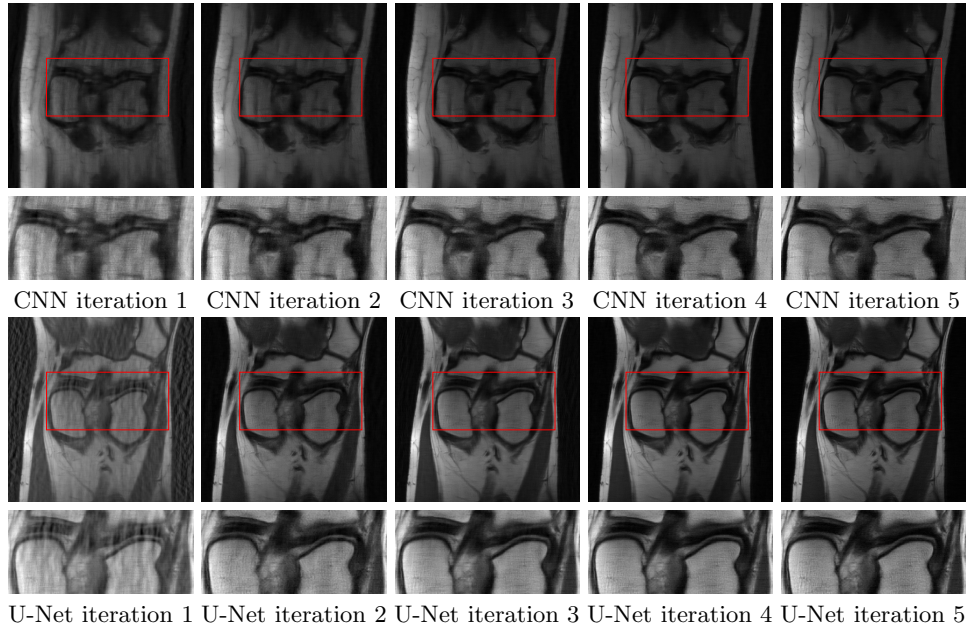


**Fig. 6.** Reconstruction images visual evolution in each iteration of unfolding structure with  $\sigma$  and their related ROIs.

The reconstruction results are demonstrated in Figs. 8 and 9. These figures also include the ground truth, ZF images, Region of Interest (ROI), and error map. Apparently, the proposed unfolding structures are recovered more patterns and presented richer perceptual quality. Furthermore, the suggested designs' output images have fewer significant artifacts and the majority of the blurring issues have been addressed. As can be observed, the quantitative findings in Tables 3 and 4 match the reconstruction results in Figs. 8 and 9.

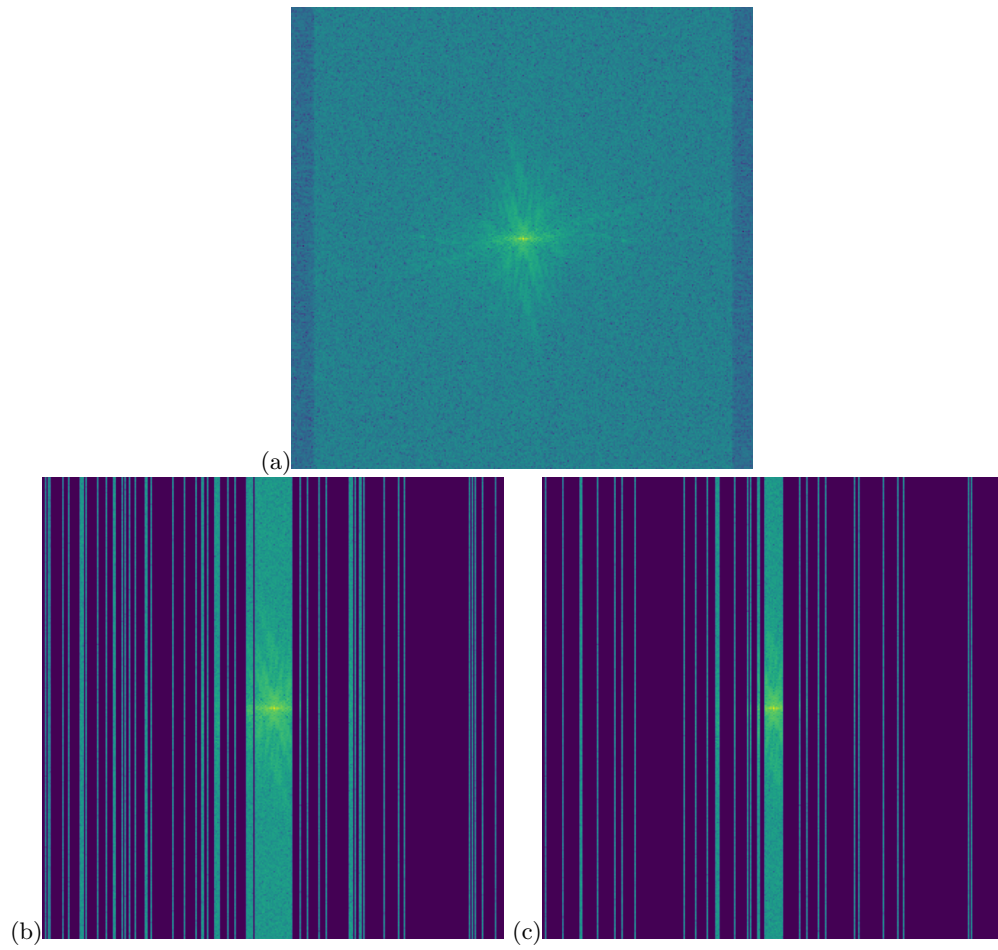


**Fig. 7.** Specific slice representations: (a) k-space, (b) subsampled k-space slice with 4-fold random Cartesian mask, (c) subsampled k-space slice with 8-fold random Cartesian mask.

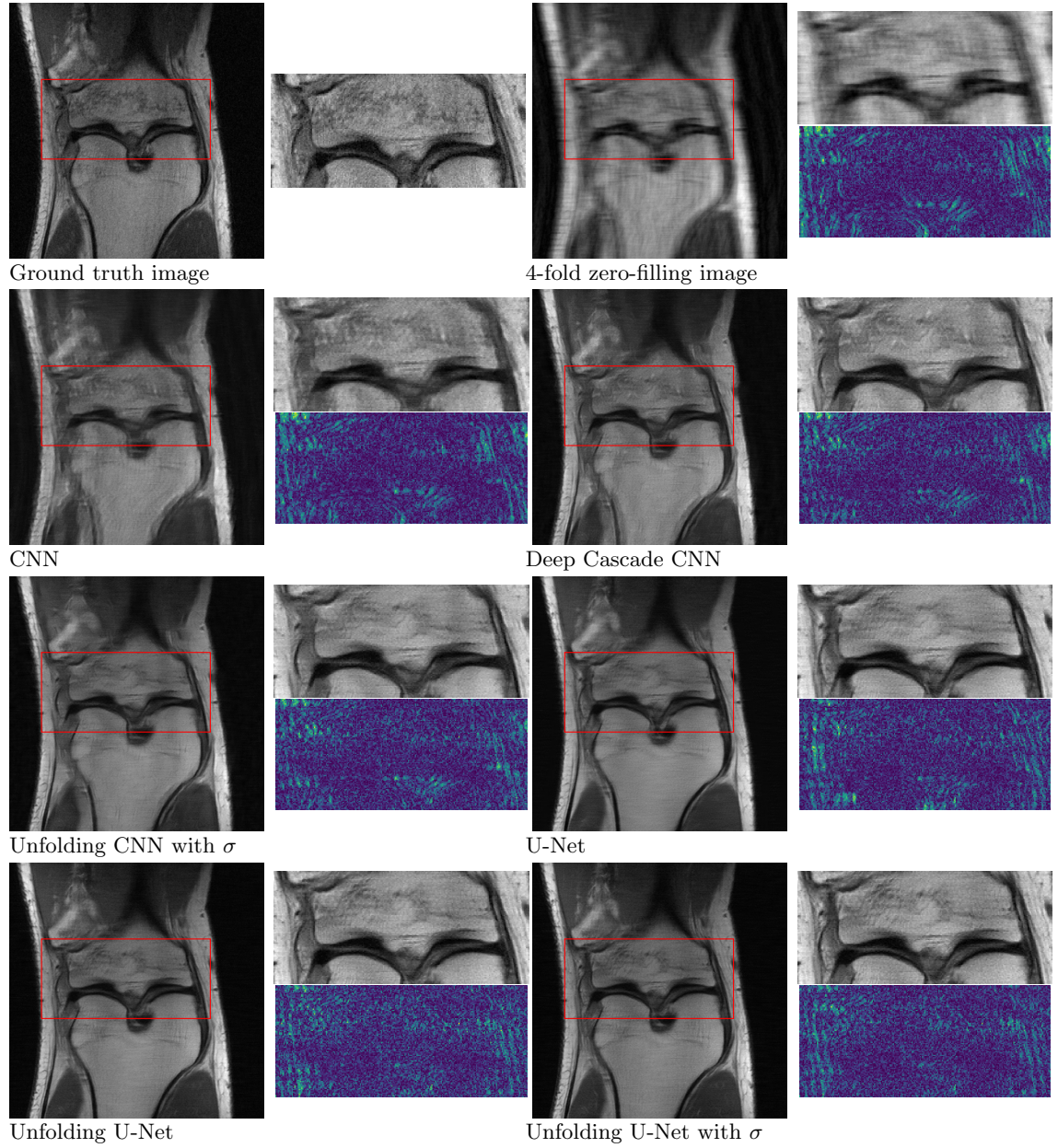


**Fig. 8.** Proposed techniques' and contender networks' reconstructed images, ROI, and error map for 4-fold undersampled slices.

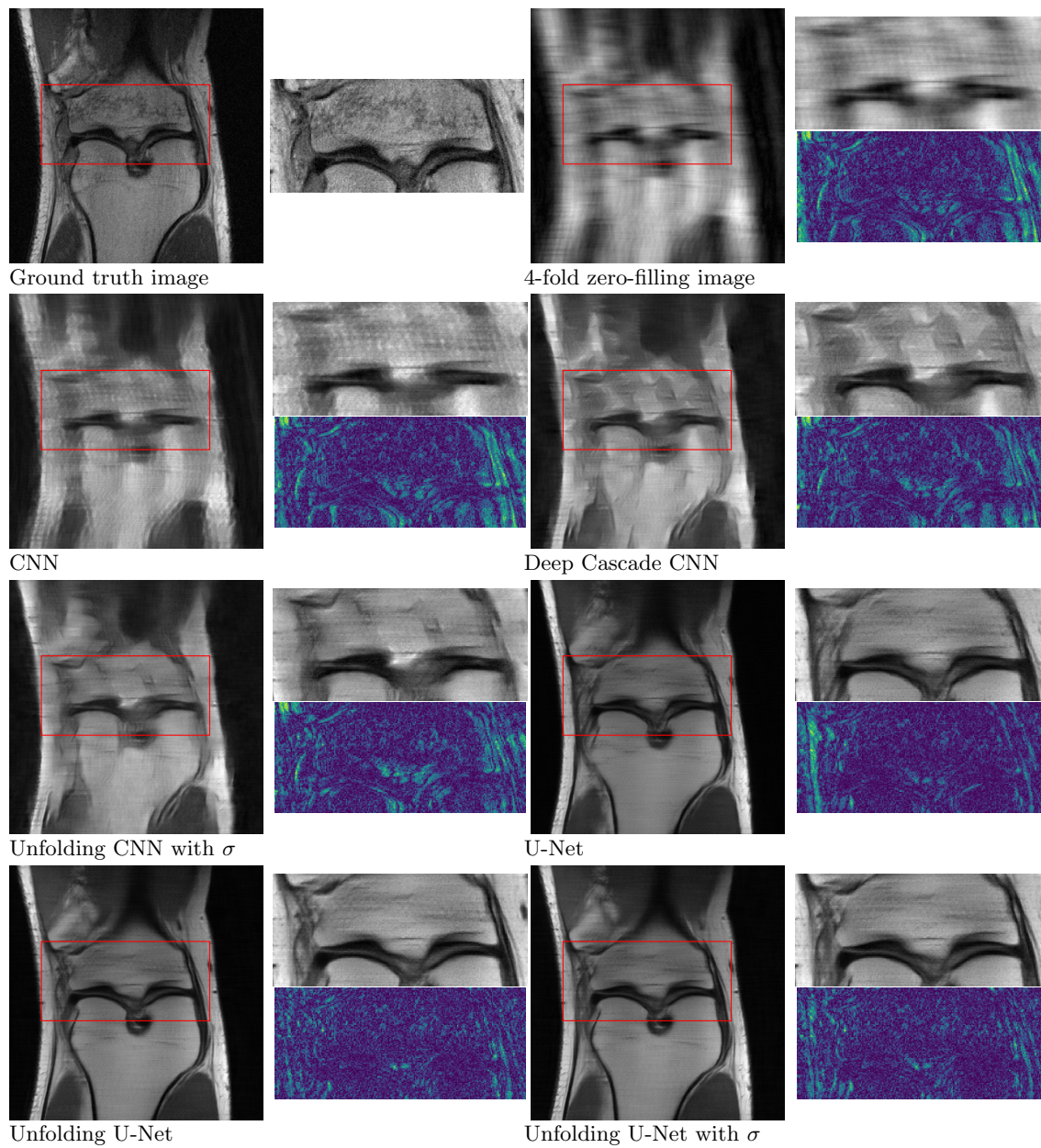


**Fig. 9.** Proposed techniques' and contender networks' reconstructed images, ROI, and error maps for 8-fold undersampled slices.

## 5 Conclusion

In recent literature, deep networks have proven their effectiveness in solving medical imaging issues. Furthermore, unfolding structures have given promising results for MRI reconstruction as indicated in cascaded and plug-and-play structures. Inspired by this fact, we introduced a novel noise parameter  $\sigma$  to the unfolding pipeline. The proposed model improves the performance of the unfolding structures without leading to any significant complexity increase. The adoption of an adaptively calculated noise level parameter at the input of the network results in better reconstruction performance. We conducted comparisons among models using quantitative and qualitative results. According to the presented findings, the offered trainable parameter boosts the unfolding structure outcomes. Using the ANOVA Single Factor approach, the statistical differences between created methodologies are emphasized. A  $t$ -test is also used to indicate the significant margin between the two suggested structures' means. In future work, the effectiveness of this proposed parameter can be tested by applying it to model-based structures or even by evaluating its performance in other image restoration problems such as tomographic reconstruction.

## Acknowledgment

This work was supported by TUBITAK (The Scientific and Technological Research Council of Turkey) under project no. 119E248.

## References

1. Adler, J., Öktem, O.: Solving ill-posed inverse problems using iterative deep neural networks. *Inverse Problems* **33**(12), 124007 (2017)
2. Aggarwal, H.K., Mani, M.P., Jacob, M.: MoDL: Model-based deep learning architecture for inverse problems. *IEEE Transactions on Medical Imaging* **38**(2), 394–405 (2018)
3. Aghabiglou, A., Eksioğlu, E.M.: Projection-Based cascaded U-Net model for MR image reconstruction. *Computer Methods and Programs in Biomedicine* **207**, 106151 (2021)
4. Boyd, S., Parikh, N., Chu, E.: *Distributed optimization and statistical learning via the alternating direction method of multipliers*. Now Publishers Inc (2011)
5. Chaâri, L., Pesquet, J.C., Benazza-Benyahia, A., Ciuciu, P.: A wavelet-based regularized reconstruction algorithm for SENSE parallel MRI with applications to neuroimaging. *Medical Image Analysis* **15**(2), 185–201 (2011)
6. Chen, F., Taviani, V., Malkiel, I., Cheng, J.Y., Tamir, J.I., Shaikh, J., Chang, S.T., Hardy, C.J., Pauly, J.M., Vasanawala, S.S.: Variable-density single-shot fast spin-echo MRI with deep learning reconstruction by using variational networks. *Radiology* **289**(2), 366–373 (2018)
7. Chen, L.C., Papandreou, G., Kokkinos, I., Murphy, K., Yuille, A.L.: DeepLab: Semantic Image Segmentation with Deep Convolutional Nets, Atrous Convolution, and Fully Connected CRFs. *IEEE Transactions on Pattern Analysis and Machine Intelligence* **40**(4), 834–848 (2018). <https://doi.org/10.1109/TPAMI.2017.2699184>

8. D. Kocanaogullari and E. M. Eksioğlu: Deep Learning for MRI Reconstruction Using a Novel Projection Based Cascaded Network. In: 2019 IEEE 29th International Workshop on Machine Learning for Signal Processing (MLSP) (Oct 2019). <https://doi.org/10.1109/MLSP.2019.8918715>
9. Duan, J., Schlemper, J., Qin, C., Ouyang, C., Bai, W., Biffi, C., Bello, G., Statton, B., O'regan, D.P., Rueckert, D.: VS-Net: Variable splitting network for accelerated parallel MRI reconstruction. In: International Conference on Medical Image Computing and Computer-Assisted Intervention. pp. 713–722. Springer (2019)
10. Eksioğlu, E.M., Tanc, A.K.: Denoising AMP for MRI Reconstruction: BM3D-AMP-MRI. *SIAM Journal on Imaging Sciences* **11**(3), 2090–2109 (2018). <https://doi.org/10.1137/18M1169655>, <https://doi.org/10.1137/18M1169655>
11. Eo, T., Jun, Y., Kim, T., Jang, J., Lee, H.J., Hwang, D.: KIKI-net: cross-domain convolutional neural networks for reconstructing undersampled magnetic resonance images. *Magnetic Resonance in Medicine* **80**(5), 2188–2201 (2018)
12. Goodfellow, I.J., Pouget-Abadie, J., Mirza, M., Xu, B., Warde-Farley, D., Ozair, S., Courville, A., Bengio, Y.: Generative adversarial networks. arXiv preprint arXiv:1406.2661 (2014)
13. Griswold, M.A., Jakob, P.M., Heidemann, R.M., Nittka, M., Jellus, V., Wang, J., Kiefer, B., Haase, A.: Generalized autocalibrating partially parallel acquisitions (GRAPPA). *Magnetic Resonance in Medicine: An Official Journal of the International Society for Magnetic Resonance in Medicine* **47**(6), 1202–1210 (2002)
14. Haldar, J.P., Zhuo, J.: P-LORAKS: low-rank modeling of local k-space neighborhoods with parallel imaging data. *Magnetic Resonance in Medicine* **75**(4), 1499–1514 (2016)
15. Hammernik, K., Klatzer, T., Kobler, E., Recht, M.P., Sodickson, D.K., Pock, T., Knoll, F.: Learning a variational network for reconstruction of accelerated MRI data. *Magnetic Resonance in Medicine* **79**(6), 3055–3071 (2018)
16. Han, Y., Sunwoo, L., Ye, J.C.:  $k$ -Space Deep Learning for Accelerated MRI. *IEEE Transactions on Medical Imaging* **39**(2), 377–386 (Feb 2019). <https://doi.org/10.1109/TMI.2019.2927101>
17. Hollingsworth, K.G.: Reducing acquisition time in clinical MRI by data undersampling and compressed sensing reconstruction. *Physics in Medicine and Biology* **60**, R297–R322 (oct 2015). <https://doi.org/10.1088/0031-9155/60/21/r297>
18. Jifara, W., Jiang, F., Rho, S., Cheng, M., Liu, S.: Medical image denoising using convolutional neural network: a residual learning approach. *The Journal of Supercomputing* **75**(2), 704–718 (2019)
19. Krizhevsky, A., Sutskever, I., Hinton, G.E.: Imagenet classification with deep convolutional neural networks. In: *Advances in Neural Information Processing Systems*. pp. 1097–1105 (2012)
20. LeCun, Y., Bengio, Y., Hinton, G.: Deep learning. *nature* **521**(7553), 436–444 (2015)
21. LeCun, Y., Boser, B., Denker, J.S., Henderson, D., Howard, R.E., Hubbard, W., Jackel, L.D.: Backpropagation applied to handwritten zip code recognition. *Neural Computation* **1**(4), 541–551 (1989)
22. Lee, D., Yoo, J., Ye, J.C.: Deep residual learning for compressed sensing MRI. In: 2017 IEEE 14th International Symposium on Biomedical Imaging (ISBI 2017). pp. 15–18 (2017). <https://doi.org/10.1109/ISBI.2017.7950457>
23. Lee, D., Lee, J., Ko, J., Yoon, J., Ryu, K., Nam, Y.: Deep learning in MR image processing. *Investigative Magnetic Resonance Imaging* **23**(2), 81–99 (2019). <https://doi.org/10.13104/imri.2019.23.2.81>

24. Li, S., Chen, Y., Yang, S., Luo, W.: Cascade Dense-UNet for Prostate Segmentation in MR Images. In: Huang, D.S., Bevilacqua, V., Premaratne, P. (eds.) *Intelligent Computing Theories and Application*. pp. 481–490. Springer International Publishing, Cham (2019)
25. Liang, D., Cheng, J., Ke, Z., Ying, L.: Deep Magnetic Resonance Image Reconstruction: Inverse Problems Meet Neural Networks. *IEEE Signal Processing Magazine* **37**(1), 141–151 (2020). <https://doi.org/10.1109/MSP.2019.2950557>
26. Liang, Z.P., Madore, B., Glover, G.H., Pelc, N.J.: Fast algorithms for GS-model-based image reconstruction in data-sharing Fourier imaging. *IEEE transactions on medical imaging* **22**(8), 1026–1030 (2003)
27. Lustig, M., Donoho, D.L., Santos, J.M., Pauly, J.M.: Compressed Sensing MRI. *IEEE Signal Processing Magazine* **25**(2), 72–82 (2008). <https://doi.org/10.1109/MSP.2007.914728>
28. Mardani, M., Gong, E., Cheng, J.Y., Vasanawala, S.S., Zaharchuk, G., Xing, L., Pauly, J.M.: Deep generative adversarial neural networks for compressive sensing MRI. *IEEE Transactions on Medical Imaging* **38**(1), 167–179 (2019). <https://doi.org/10.1109/TMI.2018.2858752>
29. Pruessmann, K.P., Weiger, M., Scheidegger, M.B., Boesiger, P.: SENSE: sensitivity encoding for fast MRI. *Magnetic Resonance in Medicine: An Official Journal of the International Society for Magnetic Resonance in Medicine* **42**(5), 952–962 (1999)
30. Qiao, X., Du, J., Wang, L., He, Z., Jia, Y.: A Model-Based Deep Network for MRI Reconstruction Using Approximate Message Passing Algorithm. In: *ICASSP 2020-2020 IEEE International Conference on Acoustics, Speech and Signal Processing (ICASSP)*. pp. 1105–1109. IEEE (2020)
31. Qin, C., Schlemper, J., Caballero, J., Price, A.N., Hajnal, J.V., Rueckert, D.: Convolutional recurrent neural networks for dynamic MR image reconstruction. *IEEE transactions on medical imaging* **38**(1), 280–290 (2018)
32. Quan, T.M., Nguyen-Duc, T., Jeong, W.K.: Compressed sensing MRI reconstruction using a generative adversarial network with a cyclic loss. *IEEE Transactions on Medical Imaging* **37**(6), 1488–1497 (2018). <https://doi.org/10.1109/TMI.2018.2820120>
33. Ramzi, Z., Ciuciu, P., Starck, J.L.: Benchmarking deep nets MRI reconstruction models on the fastMRI publicly available dataset. In: *2020 IEEE 17th International Symposium on Biomedical Imaging (ISBI)*. pp. 1441–1445. IEEE (2020)
34. Ronneberger, O., Fischer, P., Brox, T.: U-Net: Convolutional Networks for Biomedical Image Segmentation. In: *Medical Image Computing and Computer-Assisted Intervention – MICCAI 2015*. pp. 234–241. Springer, Springer International Publishing (2015)
35. Schlemper, J., Caballero, J., Hajnal, J.V., Price, A., Rueckert, D.: A deep cascade of convolutional neural networks for MR image reconstruction. In: *International Conference on Information Processing in Medical Imaging*. pp. 647–658. Springer (2017)
36. Schlemper, J., Caballero, J., Hajnal, J.V., Price, A.N., Rueckert, D.: A Deep Cascade of Convolutional Neural Networks for Dynamic MR Image Reconstruction. *IEEE Transactions on Medical Imaging* **37**(2), 491–503 (2017). <https://doi.org/10.1109/TMI.2017.2760978>
37. Sodickson, D.K., Manning, W.J.: Simultaneous acquisition of spatial harmonics (SMASH): fast imaging with radiofrequency coil arrays. *Magnetic Resonance in Medicine* **38**(4), 591–603 (1997)

38. Souza, R., Bento, M., Nogovitsyn, N., Chung, K.J., Loos, W., Lebel, R.M., Frayne, R.: Dual-domain cascade of U-nets for multi-channel magnetic resonance image reconstruction. *Magnetic Resonance Imaging* **71**, 140–153 (2020)
39. Tanc, A.K., Eksioğlu, E.M.: MRI reconstruction with joint global regularization and transform learning. *Computerized Medical Imaging and Graphics* **53**, 1–8 (2016). <https://doi.org/https://doi.org/10.1016/j.compmedimag.2016.06.004>, <https://www.sciencedirect.com/science/article/pii/S0895611116300520>
40. Taud, H., Mas, J.: Multilayer perceptron (MLP). In: *Geomatic Approaches for Modeling Land Change Scenarios*, pp. 451–455. Springer (2018)
41. Wang, S., Su, Z., Ying, L., Peng, X., Zhu, S., Liang, F., Feng, D., Liang, D.: Accelerating magnetic resonance imaging via deep learning. In: *2016 IEEE 13th International Symposium on Biomedical Imaging (ISBI)*. pp. 514–517. IEEE (2016)
42. Wang, S., Xiao, T., Liu, Q., Zheng, H.: Deep learning for fast MR imaging: A review for learning reconstruction from incomplete k-space data. *Biomedical Signal Processing and Control* **68**, 102579 (2021). <https://doi.org/https://doi.org/10.1016/j.bspc.2021.102579>
43. Wei, K., Aviles-Rivero, A., Liang, J., Fu, Y., Schönlieb, C.B., Huang, H.: Tuning-free Plug-and-Play Proximal Algorithm for Inverse Imaging Problems. In: III, H.D., Singh, A. (eds.) *Proceedings of the 37th International Conference on Machine Learning. Proceedings of Machine Learning Research*, vol. 119, pp. 10158–10169. PMLR (13–18 Jul 2020)
44. Wu, J., Liu, F., Jiao, L., Wang, X., Hou, B.: Multivariate compressive sensing for image reconstruction in the wavelet domain: using scale mixture models. *IEEE Transactions on Image Processing* **20**(12), 3483–3494 (2011)
45. Wu, Y., Ma, Y., Liu, J., Du, J., Xing, L.: Self-attention convolutional neural network for improved MR image reconstruction. *Information Sciences* **490**, 317–328 (2019). <https://doi.org/https://doi.org/10.1016/j.ins.2019.03.080>, <http://www.sciencedirect.com/science/article/pii/S0020025519302919>
46. Yuan, Y., Qin, W., Guo, X., Buyyounouski, M., Hancock, S., Han, B., Xing, L.: Prostate Segmentation with Encoder-Decoder Densely Connected Convolutional Network (Ed-Densenet). In: *2019 IEEE 16th International Symposium on Biomedical Imaging (ISBI 2019)*. pp. 434–437 (2019). <https://doi.org/10.1109/ISBI.2019.8759498>
47. Zbontar, J., Knoll, F., Sriram, A., Muckley, M.J., Bruno, M., Defazio, A., Parente, M., Geras, K.J., Katsnelson, J., Chandarana, H., et al.: fastMRI: An open dataset and benchmarks for accelerated MRI. *arXiv preprint arXiv:1811.08839* (2018)
48. Zhang, J., Ghanem, B.: ISTA-Net: Interpretable optimization-inspired deep network for image compressive sensing. In: *Proceedings of the IEEE conference on computer vision and pattern recognition*. pp. 1828–1837 (2018)
49. Zhang, K., Li, Y., Zuo, W., Zhang, L., Gool, L.V., Timofte, R.: Plug-and-Play Image Restoration with Deep Denoiser Prior. *IEEE Transactions on Pattern Analysis and Machine Intelligence* (2021). <https://doi.org/10.1109/TPAMI.2021.3088914>
50. Zhang, K., Zuo, W., Chen, Y., Meng, D., Zhang, L.: Beyond a Gaussian Denoiser: Residual Learning of Deep CNN for Image Denoising. *IEEE Transactions on Image Processing* **26**(7), 3142–3155 (2017). <https://doi.org/10.1109/TIP.2017.2662206>
51. Zhang, K., Zuo, W., Zhang, L.: FFDNet: Toward a fast and flexible solution for CNN-Based image denoising. *IEEE Transactions on Image Processing* **27**, 4608–4622 (9 2018). <https://doi.org/10.1109/TIP.2018.2839891>